One-dimensional textures and critical velocity in superfluid ³He-A

J. Kopu, R. Hänninen, and E. V. Thuneberg

Low Temperature Laboratory, Helsinki University of Technology, 02150 Espoo, Finland

(Received 14 March 2000)

We study theoretically the stability of flow in superfluid ³He-A. The calculations are done using a one-dimensional model where the order parameter depends only on the coordinate in the direction of the superfluid velocity $\mathbf{v}_s$. We concentrate on the case that the external magnetic field $\mathbf{H}$ is perpendicular to $\mathbf{v}_s$, where only a few results are available analytically. We calculate the critical velocity v_c at which the superflow becomes unstable against the formation of continuous vortices. The detailed dependence of v_c on the temperature and on the form of the underlying orbital texture $\hat{\mathbf{l}}(\mathbf{r})$ is investigated. Both uniform and helical textures of $\hat{\mathbf{l}}$ and two types of domain-wall structures are studied. The results are partially in agreement with experiments made in a rotating cylinder.

I. INTRODUCTION

The superflow of ³He-A differs markedly from the well known superfluid ⁴He, where the decay of persistent currents is limited by topological constraints. The circulation of the superfluid velocity $\mathbf{v}_s$ on a closed contour is not quantized in ³He-A, but depends on the field $\hat{\mathbf{l}}(\mathbf{r})$ of the orbital anisotropy vector. Thus ³He-A can respond to externally applied flow by forming an inhomogeneous texture of $\hat{\mathbf{l}}(\mathbf{r})$. The rigidity of the order parameter stabilizes the uniform bulk state [with $\hat{\mathbf{l}}(\mathbf{r}) = $ const] for small flow velocities in most cases, depending on the magnitude and direction of the external magnetic field $\mathbf{H}$. With increasing velocity this configuration becomes unstable against textural inhomogeneities that finally lead to the formation of "continuous" vortices. In several cases a helical texture of $\hat{\mathbf{l}}(\mathbf{r})$ is stabilized at intermediate velocities.

The flow properties of bulk ³He-A were studied in many theoretical papers which peaked in the late 1970s.[1–12] The majority of that work studied the case where the superfluid velocity and the magnetic field are parallel. Various methods were used to generate the flow experimentally (torsional oscillator, thermal gradient, a piston, etc.; see Refs. 13 and 14 for reviews). Although some of the predicted features were seen in the experiments, no satisfactory agreement between theory and experiment was found.

More recently, a rotating cryostat has been used to generate superflow.[15] This method gives a well-defined dc superfluid velocity under very steady conditions. These experiments motivated our theoretical studies. First, it was necessary to study the case where $\mathbf{v}_s$ is perpendicular to $\mathbf{H}$. The helical texture in this case was previously considered only in one paper.[4] Second, the calculation has to be generalized to temperatures substantially below the superfluid transition temperature T_c. Third, we consider two different types of "solitons." These are domain-wall-like structures whose effect on the flow properties were previously considered in a few cases.[3,5,10–12] Here we present detailed calculations of the critical velocities v_c for the appearance of helical textures and of vortices in different cases with $\mathbf{v}_s \perp \mathbf{H}$. The comparison of the results with experimental measurements has been given before.[15]

The hydrodynamic free energy describing the current-carrying states of ³He-A is recalled in Sec. II. In Sec. III we study the general features of our one-dimensional (1D) model and its numerical solution. Section IV discusses the instabilities of uniform and helical textures. In Sec. V the critical velocity associated with two initially inhomogeneous textures, a dipole-locked and a dipole-unlocked soliton, is investigated. The comparison to experiments is briefly discussed in Sec. VI.

II. HYDROSTATIC THEORY

The order parameter of ³He-A is fully specified by defining an orthonormal triad $\{\hat{\mathbf{m}}, \hat{\mathbf{n}}, \hat{\mathbf{l}}\}$ and a unit vector $\hat{\mathbf{d}}$. The triad describes the orbital part and $\hat{\mathbf{d}}$ the spin part of the tensor order parameter[16]

$$A_{\mu j} = \Delta \hat{d}_\mu (\hat{m}_j + i\hat{n}_j). \tag{1}$$

Here Δ is a (temperature-dependent) constant and $\hat{\mathbf{l}} \equiv \hat{\mathbf{m}} \times \hat{\mathbf{n}}$. All the unit vectors may vary as functions of location $\mathbf{r}$. A change in the total phase Φ of the order parameter (1) is given by

$$\delta\Phi = \frac{1}{2} \sum_j [\hat{m}_j \delta\hat{n}_j - \hat{n}_j \delta\hat{m}_j] = \sum_j \hat{m}_j \delta\hat{n}_j. \tag{2}$$

This allows for the definition for the superfluid velocity as

$$\mathbf{v}_s = \frac{\hbar}{2m} \sum_j \hat{m}_j \boldsymbol{\nabla} \hat{n}_j, \tag{3}$$

where m in the prefactor is the mass of a ³He atom. The equilibrium properties of the superfluid are determined by the order-parameter configuration that minimizes the total free energy. In the hydrodynamic approximation it has the form

$$F = \int d^3\mathbf{r} f = \int d^3\mathbf{r}(f_{gr} + f_d + f_h). \tag{4}$$

The gradient energy density can be written as

$$f_{gr} = \frac{1}{2}\rho_\perp \mathbf{v}_s^2 + \frac{1}{2}(\rho_\parallel - \rho_\perp)(\hat{\mathbf{l}} \cdot \mathbf{v}_s)^2 + C\mathbf{v}_s \cdot \nabla \times \hat{\mathbf{l}} - C_0(\hat{\mathbf{l}} \cdot \mathbf{v}_s)$$

$$\times (\hat{\mathbf{l}} \cdot \nabla \times \hat{\mathbf{l}}) + \frac{1}{2}K_s(\nabla \cdot \hat{\mathbf{l}})^2 + \frac{1}{2}K_t(\hat{\mathbf{l}} \cdot \nabla \times \hat{\mathbf{l}})^2$$

$$+ \frac{1}{2}K_b|\hat{\mathbf{l}} \times (\nabla \times \hat{\mathbf{l}})|^2 + \frac{1}{2}K_5|(\hat{\mathbf{l}} \cdot \nabla)\hat{\mathbf{d}}|^2$$

$$+ \frac{1}{2}K_6 \sum_{ij} [(\hat{\mathbf{l}} \times \nabla)_i \hat{\mathbf{d}}_j]^2. \qquad (5)$$

The first four terms give the kinetic energy of the anisotropic superfluid. The C and C_0 terms give the coupling between flow and an inhomogeneous $\hat{\mathbf{l}}$ field. The remaining five terms are the bending energy densities for $\hat{\mathbf{l}}$ and $\hat{\mathbf{d}}$.

The energy density of the dipole-dipole interaction is

$$f_d = -\frac{1}{2}\lambda_d(\hat{\mathbf{d}} \cdot \hat{\mathbf{l}})^2. \qquad (6)$$

Comparing this to the kinetic energy (5) defines the dipole velocity $v_d = \sqrt{\lambda_d/\rho_\parallel} \sim 1$ mm/s and the dipole length $\xi_d = \hbar/2mv_d \sim 10$ μm. In addition, the energy density in the presence of an external magnetic field $\mathbf{H}$ is

$$f_h = \frac{1}{2}\lambda_h(\hat{\mathbf{d}} \cdot \mathbf{H})^2. \qquad (7)$$

It is customary to define the dipole field $H_d = \sqrt{\lambda_d/\lambda_h}$, $\mu_0 H_d \sim 2$ mT, by comparing Eqs. (6) and (7).

All the coefficients $\rho_\perp$, $\rho_\parallel$, C, C_0, K_s, K_t, K_b, K_5, K_6, λ_d, and λ_h are positive and depend on the temperature T and the pressure p. Their values are determined as explained in Ref. 17. In particular, the coefficients are calculated using the weak-coupling approximation including leading Fermi-liquid corrections. In reduced units of v_d, ξ_d, and H_d our results are independent of λ_d and λ_h, but they are needed for comparison to experiments.[15] For λ_d we write

$$\lambda_d(T,p) = 4g_D(p)\Delta_A^2(T,p), \qquad (8)$$

where Δ_A is the maximum energy gap in the weak-coupling approximation. All calculations are done at the melting pressure where $g_D = 5.9 \times 10^{44}$ J^{-1} m^{-3}.[18] We wish to emphasize that the calculations contain no adjustable parameters.

The hydrostatic theory gives a good description of the superflow in ^{3}He-A over most of the temperature region $0 < T < T_c$. It becomes invalid in a small region $T_c - T \lesssim 10^{-6}T_c$ around T_c, where the Ginzburg-Landau critical velocity $\sim (\hbar/2m)\xi_{GL}^{-1}$ is smaller than v_d. We also limit to such low fields that the deformation of the A phase order parameter (1) towards the A_1 phase can be neglected.

III. ONE-DIMENSIONAL CALCULATION

We study flow in bulk ^{3}He-A far from any walls. The main assumption in the present work is that the order parameter (1) depends only on one spatial coordinate x. It follows from the definition (3) that $\mathbf{v}_s$ is always parallel to the x axis, $\mathbf{v}_s \parallel \hat{\mathbf{x}}$. In addition to the homogeneous state, the 1D model allows us to calculate the structure of helical textures and the

deformation of solitons in a flow that is perpendicular to the soliton wall. Moreover, we also can determine the stability limits of such textures against 1D perturbations. We will argue in Sec. VI that the local stability of the states we consider is indeed determined by such perturbations.

The cases of $H = 0$ (Refs. 1, 2, 7, 10, and 12) and $\mathbf{H} \parallel \hat{\mathbf{x}}$ (Refs. 3–6,8,9, and 11) have been studied extensively in the literature. Here we study the more complicated case $\mathbf{H} \perp \hat{\mathbf{x}}$.[4,5] We study in particular the high field limit $H \gg H_d$, where $\hat{\mathbf{d}} \perp \mathbf{H}$ everywhere.

The order parameter of ^{3}He-A can be parametrized by introducing three Euler angles α, β, and γ for the orbital triad $\{\hat{\mathbf{m}}, \hat{\mathbf{n}}, \hat{\mathbf{l}}\}$ and polar and azimuthal angles ψ and ϕ for $\hat{\mathbf{d}}$. In this representation one has to beware of the unphysical singularities at the poles $\sin\beta = 0$ or $\sin\psi = 0$. For this reason we choose the polar axis $\hat{\mathbf{z}}$ of the fixed coordinate system perpendicular to the direction of $\mathbf{v}_s$ (and parallel to the external magnetic field). This results in a more complicated form of the energy functional but it enables us to avoid the singularities in all stationary states. With these definitions

$$\hat{\mathbf{l}} = \sin\beta\cos\alpha\hat{\mathbf{x}} + \sin\beta\sin\alpha\hat{\mathbf{y}} + \cos\beta\hat{\mathbf{z}}, \qquad (9)$$

$$\hat{\mathbf{d}} = \sin\psi\cos\phi\hat{\mathbf{x}} + \sin\psi\sin\phi\hat{\mathbf{y}} + \cos\psi\hat{\mathbf{z}}, \qquad (10)$$

$$\mathbf{v}_s = -\frac{\hbar}{2m}\left(\frac{d\gamma}{dx} + \cos\beta\frac{d\alpha}{dx}\right)\hat{\mathbf{x}}. \qquad (11)$$

The form of the unknown functions $\alpha(x)$, $\beta(x)$, $\gamma(x)$, $\psi(x)$, and $\phi(x)$ in equilibrium corresponds to the minimum of the free energy functional (4) where

$$\frac{\delta f}{\delta\alpha} \equiv \frac{\partial f}{\partial\alpha} - \frac{d}{dx}\left[\frac{\partial f}{\partial(d\alpha/dx)}\right] = 0, \qquad (12)$$

and similarly for other angles.

We point out two analytic observations that are useful in testing the convergence and the accuracy of the numerical solution. First, the superfluid velocity $\mathbf{v}_s$, Eq. (11), and therefore also the total free energy (4) do not depend explicitly on the angle γ but only on its derivative. The corresponding Euler equation (12) reduces to a conservation law

$$\frac{\partial f}{\partial(d\gamma/dx)} \equiv -p = \text{const}. \qquad (13)$$

The quantity $(2m/\hbar)p$ is the x component of the supercurrent density

$$\mathbf{j}_s = \rho_\perp \mathbf{v}_s + (\rho_\parallel - \rho_\perp)\hat{\mathbf{l}}(\hat{\mathbf{l}} \cdot \mathbf{v}_s) + C\nabla \times \hat{\mathbf{l}} - C_0\hat{\mathbf{l}}(\hat{\mathbf{l}} \cdot \nabla \times \hat{\mathbf{l}}). \qquad (14)$$

Another conserved quantity in the problem is the one corresponding to the fact that the free energy (4) does not depend explicitly on x either. The invariant related to this is analogous to the Hamiltonian of classical mechanics and can be brought to the form

$$f_{gr} - f_d - f_h = \text{const}. \qquad (15)$$

We wish to study a one-dimensional interval of length $L \gg \xi_d$. A flow through the system is achieved by keeping a fixed phase difference $\Delta\Phi \equiv \Phi(L/2) - \Phi(-L/2)$ between

the end points of the line. The constancy of $\Delta\Phi$ as a function of time t is enforced by imposing the boundary condition

$$\frac{d\Delta\Phi}{dt} \equiv -\left(\frac{d\gamma}{dt} + \cos\beta\frac{d\alpha}{dt}\right)_{x=L/2} + \left(\frac{d\gamma}{dt} + \cos\beta\frac{d\alpha}{dt}\right)_{x=-L/2}$$

$$= 0. \tag{16}$$

It is, however, more advantageous to express the results in terms of a driving velocity defined by $v_n = (\hbar/2m)\Delta\Phi/L$. This is a more convenient quantity than $\Delta\Phi$ because all our results are independent of L when expressed in terms of v_n. Here v_n could be identified as the velocity of the normal component that drives the superfluid component of the liquid. However, v_n should be considered as a scalar parameter since all vector quantities in this paper (like $\mathbf{v}_s$ and $\mathbf{j}_s$) are given in the frame where the normal fluid is at rest, $\mathbf{v}_n \equiv 0$. (See Ref. 19 for a general formulation with $\mathbf{v}_n \neq 0$.)

In the general case we have to use numerical methods to determine the equilibrium state of the system. The order parameter is taken to be defined at N equally spaced discrete points on the line. The discretization length $\Delta x \equiv L/N$ is chosen much smaller than the dipole length, usually $\Delta x \lesssim 0.1\xi_d$. As a first step we have to choose some initial configuration for the five angles. A given $\Delta\Phi$ or v_n is implemented by taking an initial guess $\gamma(x) = (-2m/\hbar)v_n x$. The angle functions are then iterated numerically towards the equilibrium state for a given v_n using the following diffusionlike equations:

$$\mu_1 \sin^2\beta\frac{\partial\alpha}{\partial t} = -\frac{\delta f}{\delta\alpha},$$

$$\mu_1 \frac{\partial\beta}{\partial t} = -\frac{\delta f}{\delta\beta},$$

$$\mu_2 \frac{\partial\gamma}{\partial t} = -\frac{\delta f}{\delta\gamma},$$

$$\mu_3 \sin^2\psi\frac{\partial\phi}{\partial t} = -\frac{\delta f}{\delta\phi},$$

$$\mu_3 \frac{\partial\psi}{\partial t} = -\frac{\delta f}{\delta\psi}, \tag{17}$$

together with the boundary condition (16). The simplest discretized expressions have been used in representing the derivatives in Eqs. (17). Since we do not attempt to describe the true time evolution of the textures, the viscosity constants μ_1, μ_2, and μ_3 can be chosen according to numerical convenience.

IV. UNIFORM AND HELICAL TEXTURES

The simplest texture has constant $\hat{\mathbf{l}} \| \hat{\mathbf{d}} \| \hat{\mathbf{x}}$. This uniform state minimizes both the dipole-dipole energy (6) and the field energy (7) for $\mathbf{H} \perp \hat{\mathbf{x}}$. It also corresponds to the minimum of the first two terms in the gradient energy (5) because $\rho_\| < \rho_\perp$. The current in this state is linear in v_n, $\mathbf{j}_s = \rho_\| v_n \hat{\mathbf{x}}$, as illustrated in Fig. 1.

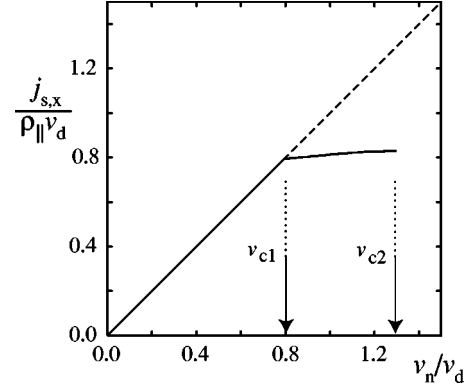The uniform state is stable at small velocities (if $H \neq 0$).

FIG. 1. The supercurrent $j_{s,x}$ as a function of driving velocity v_n at $T = 0.6T_c$ and $H \gg H_d$. The diagonal line corresponds to the current in the uniform texture, $j_s = \rho_\| v_n$. The solid line between v_{c1} and v_{c2} corresponds to helical texture at the optimal wave vector q_{opt}.

We call the stability limit of the uniform texture the first critical velocity v_{c1}. At $v_n = v_{c1}$ the uniform state becomes unstable against a helical deformation where $\hat{\mathbf{l}}$ winds around the direction of the flow; see Fig. 2. At this point the energy cost in forming an inhomogeneous texture is compensated by reductions in other energy terms. In particular, the superfluid velocity v_s, Eq. (11), is lowered for a given v_n and there is a negative contribution from the energy term with the coefficient C_0, Eq. (5).[1]

The instability point can be studied by expanding the energy (4) around the uniform solution. This calculation was done by Lin-Liu et al. in the Ginzburg-Landau region.[4] We generalize this calculation to all temperatures. We define γ as above but otherwise use a parametrization that is different from Eqs. (9)–(11):

$$\hat{\mathbf{l}} = \left[1 - \frac{1}{2}(l_y^2 + l_z^2) - \frac{1}{8}(l_y^2 + l_z^2)^2\right]\hat{\mathbf{x}} + l_y\hat{\mathbf{y}} + l_z\hat{\mathbf{z}}, \tag{18}$$

$$\hat{\mathbf{d}} = \left[1 - \frac{1}{2}(d_y^2 + d_z^2) - \frac{1}{8}(d_y^2 + d_z^2)^2\right]\hat{\mathbf{x}} + d_y\hat{\mathbf{y}} + d_z\hat{\mathbf{z}}, \tag{19}$$

$$\mathbf{v}_s = \frac{\hbar}{2m}\left\{-\frac{d\gamma}{dx} + \frac{1}{2}\left(l_y\frac{dl_z}{dx} - l_z\frac{dl_y}{dx}\right)\left[1 + \frac{1}{4}(l_y^2 + l_z^2)\right]\right\}\hat{\mathbf{x}}. \tag{20}$$

These equations are valid up to fourth order in l_y, l_z, d_y, and d_z. We eliminate $\gamma(x)$ in favor of the current p, Eq. (13), by defining a new free energy $G = F + \int dx (d\gamma/dx)p$. Substitution of Eqs. (18)–(20) into G and expansion to second order gives linear Euler-Lagrange equations. These have the solution

FIG. 2. Variation of $\hat{\mathbf{l}}$ in a helical texture as a function of x (Ref. 20). One wavelength λ of the helix is shown.

$$l_y(x) = us\sin(qx), \tag{21}$$

$$l_z(x) = (u/s)\cos(qx), \tag{22}$$

$$d_y(x) = u\delta_1 s\sin(qx), \tag{23}$$

$$d_z(x) = (u\delta_2/s)\cos(qx), \tag{24}$$

where q is the wave vector of the helix. The magnetic field in the transverse z direction introduces ''easy'' and ''hard'' directions for the amplitudes, and thus the helix has an elliptically distorted form. When G is minimized with respect to s, δ_1, and δ_2 we find

$$\delta_1 = (K_5 q^2 + 1)^{-1}, \tag{25}$$

$$\delta_2 = (K_5 q^2 + H^2 + 1)^{-1}, \tag{26}$$

$$s^2 = K_2/K_1, \tag{27}$$

$$K_i^2 = 1 + (\rho_\perp - 1)p^2 + K_b q^2 - \delta_i. \tag{28}$$

For the free energy we find the expansion

$$G = G_0 + \frac{1}{2}Au^2 + \frac{1}{4}Bu^4 \tag{29}$$

where

$$G_0 = -\frac{1}{2}(1 + p^2), \tag{30}$$

$$A = K_1 K_2 - (2C_0 + 1)qp, \tag{31}$$

$$
\begin{aligned}
B = &\left[(2\rho_\perp - 1)C_0 - \frac{1}{4}\right]\left(\frac{K_2}{K_1} + \frac{K_1}{K_2}\right)qp + \frac{1}{4}\Bigg\{ + \frac{K_2^2}{K_1^2}[3\delta_1(1-\delta_1)^2 + (K_s + (K_6 - K_5)\delta_1^2 + K_5\delta_1^4)q^2 - 3(\rho_\perp - 1)^2 p^2] \\
&+ \frac{K_2^2}{K_1^2}[3\delta_2(1-\delta_2)^2 + (K_s + (K_6 - K_5)\delta_2^2 + K_5\delta_2^4)q^2 - 3(\rho_\perp - 1)^2 p^2] + [8K_t - 2K_s - 8C_0^2 - 8K_b \\
&+ 3(K_6 - K_5)(\delta_1^2 + \delta_2^2) - 2K_5\delta_1^2\delta_2^2]q^2 + (1-\delta_1)(1-\delta_2)(\delta_1 + \delta_2) - 2(\rho_\perp - 1)^2 p^2 \Bigg\}.
\end{aligned} \tag{32}
$$

For simplicity, we have used units where $\lambda_d = \lambda_h = \rho_\parallel = \hbar/2m = 1$ in Eqs. (25)–(32). Near the superfluid transition temperature these results reduce to those by Lin-Liu et al.[4]

The uniform texture is stable if the coefficient A is positive. The line where A vanishes in the v_n–q plane is shown
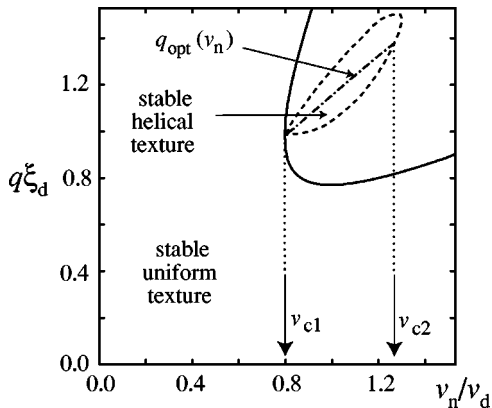

FIG. 3. The stability of different states in the v_n-q plane at $T = 0.6T_c$ and for $H \gg H_d$. The solid line marks the instability of the uniform texture according to $A(v_n,q) = 0$, Eq. (31). The helical texture is stable inside the region spanned by the dashed line. The dash-dotted line shows the optimum wave vector q_{opt} as a function of the driving velocity v_n.

by the solid line in Fig. 3. In a long interval $L \gg \xi_d$ the value of the wave vector q is not limited. This means that the uniform texture is stable only below the critical velocity v_{c1} defined by the conditions $A = \partial A/\partial q = 0$. The velocity v_{c1} is plotted as a function of magnetic field and temperature in Fig. 4. Note that v_{c1} vanishes in zero field for temperatures $T \lesssim 0.85T_c$.

The stability of small-angle helical textures is determined by the coefficient B. The helix is stable if $B > 0$ and unstable if $B < 0$. The stability as a function of T and H is indicated in Fig. 4. Near T_c the helix is stable if $H < 2.5H_d$. Lowering the temperature the stability region grows and in the temperature interval $0.5T_c$–$0.8T_c$ the helix is stable at all fields. Below $0.5T_c$ the stability region starts to shrink. Stable helices are again recovered at the lowest temperatures $\approx 0.1T_c$.

Helical textures with general opening angles were studied numerically. The periodicity of the helix allows the numerical calculations to be limited to a single wavelength $\lambda = 2\pi/q$ using periodic boundary conditions for $\hat{\mathbf{l}}$ and $\hat{\mathbf{d}}$. In fact, making use of all the symmetries even a quarter of λ would be sufficient. We then minimize the free energy (4) with respect to the five angle fields in Eqs. (9)–(11). This gives the energy as a function of v_n and q: $F(v_n, q)$.

For each value of v_n we determine the optimum wave vector q_{opt} at which the energy of the helix is minimized.
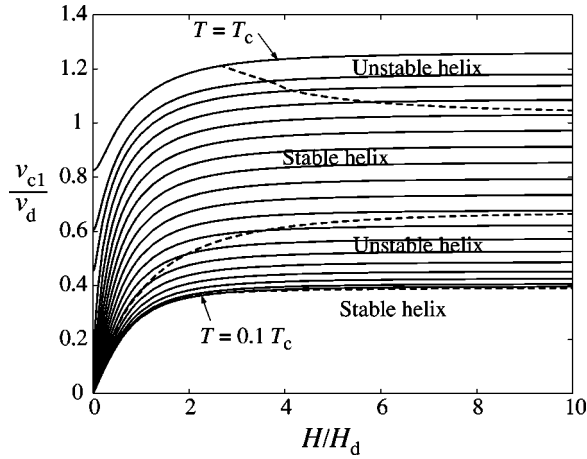
FIG. 4. The critical velocity v_{c1} of the uniform texture (solid lines) as a function of the magnetic field H. The different curves correspond to different temperatures with intervals of $0.05T_c$. The regions of stability and instability of a small-angle helix are separated by dashed lines. More details of the specific case $T=T_c$ are given in Fig. 10.

This process is simplified by the fact that the derivative of F with respect to q can be obtained using the formula

$$\frac{\partial F}{\partial q} = \frac{1}{q}(2F_{gr} - v_n J_{s,x}),\qquad (33)$$

with F_{gr} and $J_{s,x}$ defined to be the corresponding densities f_{gr} and $j_{s,x}$ integrated over the one-dimensional interval. At the optimum value $q=q_{opt}(v_n)$ the derivative given by Eq. (33) vanishes. The dependence of q_{opt} on v_n is illustrated in Fig. 3.

The stability of helical textures is determined by the eigenvalues of the Hessian matrix of $F(v_n,q)$:

$$\mathcal{H} = \begin{vmatrix} \dfrac{\partial^2 F}{\partial v_n^2} & \dfrac{\partial^2 F}{\partial v_n \partial q} \\[2ex] \dfrac{\partial^2 F}{\partial v_n \partial q} & \dfrac{\partial^2 F}{\partial q^2} \end{vmatrix}.\qquad (34)$$

A texture is stable if both the eigenvalues of the Hessian matrix are positive, and unstable otherwise. The stability region is indicated by a dashed line in Fig. 3. The velocity where the state at optimal wave vector q_{opt} becomes unstable is defined as the second critical velocity, v_{c2}. In helical texture the current increases much slower with v_n than in the uniform state (Fig. 1). Therefore, the critical current j_{c2} is substantially smaller than $\rho_\| v_{c2}$. At $H=0$ and $T\approx T_c$ we find that $v_{c2}\approx 1.28 v_d$ and $j_{c2}\approx 1.13\rho_\| v_d$ (Ref. 6). In general we find essentially no field dependence of v_{c2}, in contrast to v_{c1} which vanishes at $H=0$ when $T\lesssim 0.85T_c$. The temperature dependences of v_{c1}, v_{c2}, and j_{c2} in the high-field limit are presented in Fig. 5. At high temperatures $T>0.8T_c$ there is no stable helical texture and thus v_{c1} and v_{c2} coincide. At lower temperatures v_{c2} is seen to grow distinctly above v_{c1}. Below $0.5T_c$ helical textures again become unstable (Fig. 4).

The numerical calculation of the Hessian matrix is simplified by the fact that both first derivatives (13) and (33) are
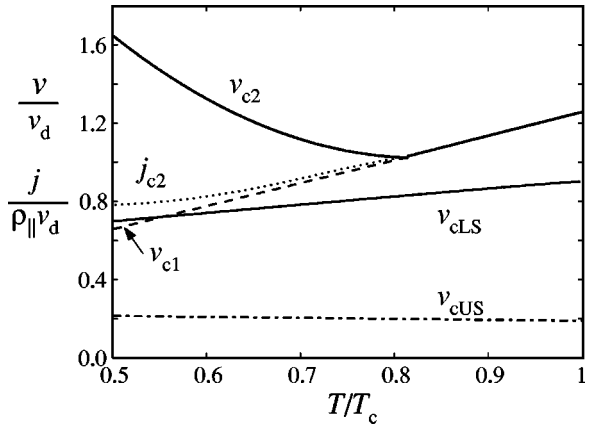

FIG. 5. The critical velocity as a function of temperature T for $H\gg H_d$. The different curves correspond to instabilities of the uniform texture v_{c1}, the helical texture v_{c2}, the locked soliton v_{cLS}, and the unlocked soliton v_{cUS}. Helical textures are stable in the region between v_{c1} and v_{c2}. The dotted line is j_{c2} in units of $\rho_\| v_d$.

easily available. Thus the calculation of the Hessian at point (v_n,q) requires texture minimizations only at three points: (v_n,q), $(v_n,q+\Delta q)$, and $(v_n+\Delta v_n,q)$. In order to minimize errors the number N of discretization points within a wavelength λ was kept constant and the discretization length $\Delta x = \lambda/N$ was varied instead.

For all helices the opening angle grows continuously from zero with increasing v_n; see Fig. 6. The largest stable values for the opening angle found in the simulations were $\sim 60\,^\circ$. We have made numerical simulations in an interval containing several wavelengths of the helix, $L\gg\lambda$. When the limit of stability is exceeded, it seems that the number of windings of the helix changes if a stable texture is possible at a given v_n. Otherwise, the instability seems to lead to the growth of the opening angle. Most likely this leads to the formation of continuous vortex structures.[19] However, we were not able to follow this process beyond 90° opening angles because of the singularity in the coordinate system (9)–(11).

V. SOLITON TEXTURES

In the previous section we studied the case where a flow was applied to an initially uniform texture. Here we investi-
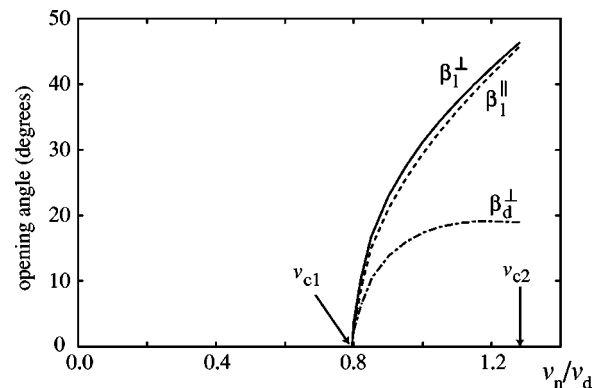

FIG. 6. The opening angles of $\hat{\mathbf{l}}$ in the plane $\perp \mathbf{H}$ ($\beta_l^\perp$, solid line) and $\|\mathbf{H}$ ($\beta_l^\|$, dashed line) and the opening angle of $\hat{\mathbf{d}}$ in the plane $\perp \mathbf{H}$ ($\beta_d^\perp$, dash-dotted line) as functions of driving velocity v_n with $q=q_{opt}$, $T=0.6T_c$, and $H\gg H_d$.
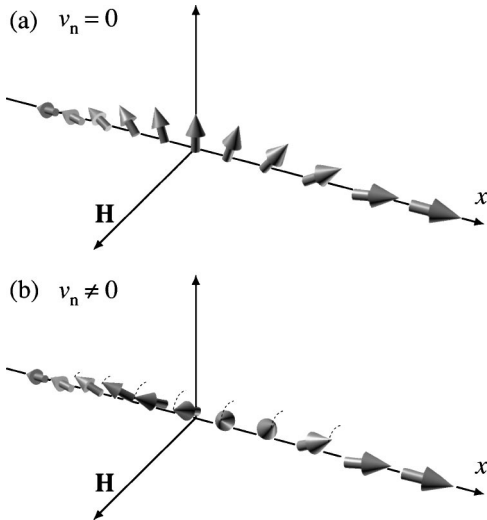
(a) $v_n = 0$

(b) $v_n \neq 0$

FIG. 7. Distribution of the vector $\hat{\mathbf{l}}$ in a one-dimensional soliton structure for $v_n = 0$ (a) and for $v_n \neq 0$ in a transverse magnetic field **H** (b) (Ref. 20). The flow tends to detach the texture from the plane $\perp$ **H**.

gate some cases where the initial state is inhomogeneous. Let us consider a texture where $\hat{\mathbf{l}}$ changes from direction $-\hat{\mathbf{x}}$ to $\hat{\mathbf{x}}$, as depicted in Fig. 7. Such a texture has the property, which follows directly from the definition (2), that if it is rotated around $\hat{\mathbf{x}}$ by angle θ, the phase difference $\Delta\Phi$ changes by 2θ. Thus, if nothing prevents the rotation of the texture, the critical current vanishes and the supercurrent is always dissipative. The presence of a magnetic field perpendicular to $\hat{\mathbf{x}}$ prefers to have $\hat{\mathbf{d}}$, and via the dipole-dipole energy (6) also $\hat{\mathbf{l}}$, in the plane perpendicular to **H**. This gives rise to a finite critical velocity that we aim to calculate.

We study two different inhomogeneous structures. The first is known as the (dipole-unlocked) soliton.[21] This is a domain-wall-like object where on one side $\hat{\mathbf{d}} = \hat{\mathbf{l}}$ and on the other side $\hat{\mathbf{d}} = -\hat{\mathbf{l}}$. Because the change between these two orientations costs dipole-dipole energy, the thickness of the
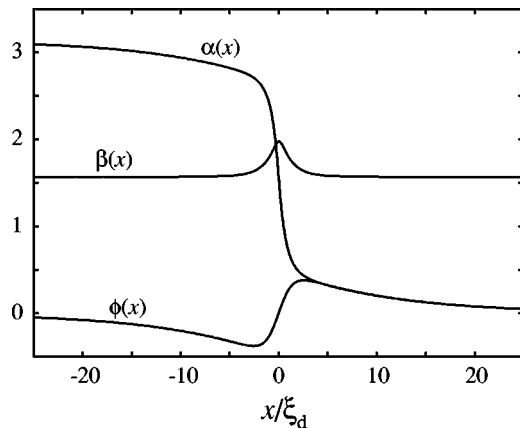

FIG. 8. The structure of the unlocked soliton at $T = T_c$, $H \gg H_d$ and $v_n = 0.15 v_d$. The angles α, β, and ϕ are defined in Eqs. (9) and (10) and $\psi = \pi/2$ because of the high-field limit. The fast change within $|x| \lesssim \xi_d$ is caused by the dipole unlocking in the soliton, and the slower change outside is caused by the anisotropy of the flow energy favoring $\hat{\mathbf{l}} = \pm \hat{\mathbf{x}}$.
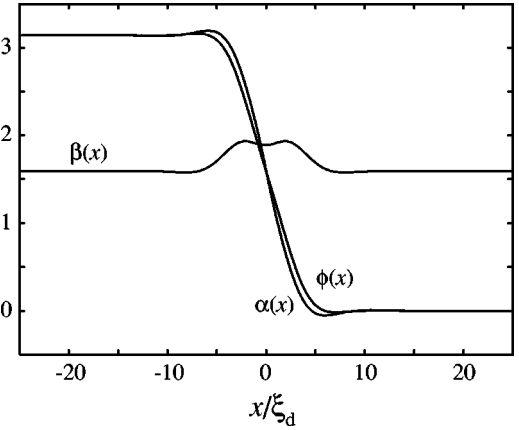

FIG. 9. The structure of the locked soliton at $T = T_c$, $H \gg H_d$ and $v_n = 0.8 v_d$. The angles α, β, and ϕ are defined in Eqs. (9) and (10) and $\psi = \pi/2$. The length scale is purely determined by the flow velocity, which here is much larger than in Fig. 8.

wall is on the order of the dipole length ξ_d. In the absence of flow the asymptotic directions of $\hat{\mathbf{l}}$ deviate from the normal $\pm \hat{\mathbf{x}}$ of the wall by an angle that depends on the temperature. When a small flow is applied perpendicular to the wall, the anisotropy of the kinetic energy $\propto -(\hat{\mathbf{l}} \cdot \mathbf{v}_s)^2$ forces the asymptotic directions of $\hat{\mathbf{l}}$ to $\pm \hat{\mathbf{x}}$. The calculated structure of the soliton is presented in Fig. 8.

The second structure we study could be called a dipole locked soliton. The dipole locking means that $\hat{\mathbf{d}}(x) \approx \hat{\mathbf{l}}(x)$ everywhere. The region where $\hat{\mathbf{l}}$ varies has finite length only in the presence of flow. The calculated structure of the locked soliton is presented in Fig. 9.

For both soliton structures the flow makes β deviate from $\pi/2$. When the flow is further increased, the structures become unstable against unlimited winding around the flow direction. The critical values of v_n are denoted by v_{cLS} for locked solitons and v_{cUS} for unlocked solitons. The critical velocities are plotted in Figs. 5 and 10. The unlocked case has previously been studied by Vollhardt and Maki[5] at $T \approx T_c$ using a variational approach. Our calculations give a much lower critical velocity than theirs. We note that the same process that leads to v_{cUS} also determines the critical
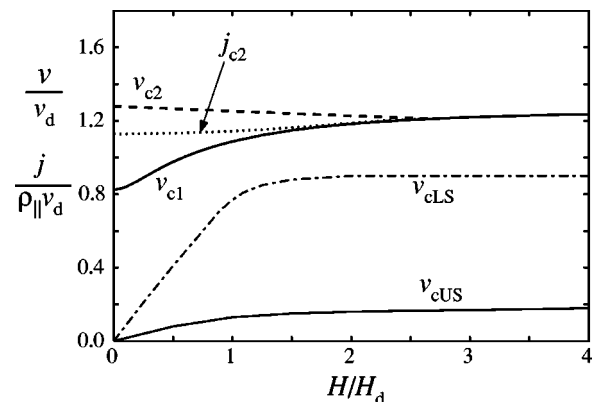

FIG. 10. The critical velocities of the locked soliton v_{cLS} and the unlocked soliton v_{cUS} as a function of the magnetic field H at temperature $T \approx T_c$. For comparison, we show also v_{c1}, v_{c2}, and $j_{c2}/\rho_\parallel$ (Fig. 4).

velocity of a vortex sheet.[22,23] The locked soliton has previously been studied only for $H=0$ or $\mathbf{H} \| \mathbf{v}_s$, where the critical velocity vanishes and only dissipative state exists.[3,10–12]

In the simulations the length L of the computational region has to be chosen large in comparison to $\xi_d v_d / v_n$. The fast variation in the unlocked soliton sets an upper limit for the discretization length, which was typically chosen as $0.1 \xi_d$. If L is not very long, the correct procedure is to extract the critical current j_{cLS} (and j_{cUS}) from the numerical calculation and then find the critical velocity using $v_{cLS} = j_{cLS}/\rho_\|$ (and $v_{cUS} = j_{cUS}/\rho_\|$).

VI. CONCLUSIONS

We have studied different 1D textures and determined their stability against 1D perturbations. It is reasonable to ask if limiting to 1D perturbations is sufficient to determine the local stability. Namely, we know at least one situation in ^{3}He-A where this is not the case: uniform $\hat{\mathbf{l}} \perp \mathbf{H} \| \hat{\mathbf{x}}$. Here the 1D model above gives stability until $v_{c1} = v_{c2} = \sqrt{\lambda_d/(\rho_\perp - \rho_\|)}$ (for $H \gg H_d$), but allowing $\mathbf{v}_s$ to deviate from the direction of the applied phase difference gives instability at v_n that is by a factor of $\sqrt{\rho_\|/\rho_\perp}$ lower.[9] This situation differs, however, from the ones studied in the previous sections. For a homogeneous texture with $\mathbf{H} \perp \hat{\mathbf{x}}$ there exists a strict proof that only 1D perturbations are relevant.[4] For helical and soliton textures the 1D model allows a natural decay mechanism for the current, and we are not aware of any mechanism that could give a lower critical velocity. Therefore we believe that other than 1D perturbations are unimportant for the helical and soliton textures studied above, although a strict proof remains open.

Measurements of the critical velocity are done by Ruutu et al.[15] They study ^{3}He-A in a circular cylinder that is rotated around its axis. In the vortex-free container the relevant driving velocity $v_n = \Omega R$, where Ω is the angular velocity and R the radius of the cylinder. Because $R \gg \xi_d$, the flow near the cylindrical wall is one dimensional to a good approximation. The magnetic field along the axis of the cylinder corresponds to a transverse field relative to the flow along the whole perimeter of the cylinder, and thus the calculations presented above should apply to this case. If the field is perpendicular to the axis, all possible angles exist between the field and flow. In this case the critical velocity of the ''uniform'' texture is determined by the orientation $\mathbf{H} \| \mathbf{v}_s$,[9] which gives a lower value of v_{c2} than $\mathbf{H} \perp \mathbf{v}_s$.

Ruutu et al. find a considerable spread in the critical velocities. On the one hand, our largest calculated values of v_c correspond to the instability of the helical texture and coincide relatively well with the largest values observed in the experiments. On the other hand, the lowest measured critical velocities can be explained by assuming the presence of a dipole-unlocked soliton. Quantitative comparison is given by Ruutu et al.[15] The comparison supports the basic assumption that the critical velocity in superfluid ^{3}He-A indicates an instability of the bulk, and it depends on the underlying texture. The bulk critical velocity is quantitatively better understood in superfluid ^{3}He-A than in any other superfluid.

[1] P. Bhattacharyya, T.-L. Ho, and N.D. Mermin, Phys. Rev. Lett. **39**, 1290 (1977).

[2] M.C. Cross and M. Liu, J. Phys. C **11**, 1795 (1978).

[3] J.R. Hook and H.E. Hall, J. Phys. C **12**, 783 (1979).

[4] Y.R. Lin-Liu, D. Vollhardt, and K. Maki, Phys. Rev. B **20**, 159 (1979).

[5] D. Vollhardt and K. Maki, Phys. Rev. B **20**, 963 (1979); **23**, 1489(E) (1981).

[6] D. Vollhardt, Y.R. Lin-Liu, and K. Maki, J. Low Temp. Phys. **37**, 627 (1979).

[7] A.L. Fetter, Phys. Rev. B **20**, 303 (1979).

[8] A.L. Fetter and M.R. Williams, Phys. Rev. Lett. **43**, 1601 (1979); Phys. Rev. B **23**, 2186 (1981).

[9] A.L. Fetter, Phys. Rev. B **24**, 1181 (1981); J. Low Temp. Phys. **48**, 435 (1982).

[10] R.C.M. Dow and J.R. Hook, Phys. Rev. Lett. **55**, 2305 (1985).

[11] R.C.M. Dow and C.J. Lambert, Jpn. J. Appl. Phys., Part 1 **26**, 201 (1987).

[12] A.L. Fetter, J. Low Temp. Phys. **70**, 499 (1988).

[13] H.E. Hall and J.R. Hook, in *Progress in Low Temperature Physics*, edited by D.F. Brewer (North-Holland, Amsterdam, 1986), Vol. IX, p. 143.

[14] H.M. Bozler, in *Helium Three*, edited by W.P. Halperin and L.P. Pitaevskii (North-Holland, Amsterdam, 1990), p. 695.

[15] V.M.H. Ruutu, J. Kopu, M. Krusius, Ü. Parts, B. Plaçais, E.V. Thuneberg, and W. Xu, Phys. Rev. Lett. **79**, 5058 (1997).

[16] D. Vollhardt and P. Wölfle, *The Superfluid Phases of Helium 3* (Taylor & Francis, London, 1990).

[17] Ü. Parts, V.M.H. Ruutu, J.H. Koivuniemi, M. Krusius, E.V. Thuneberg, and G.E. Volovik, Physica B **210**, 311 (1995).

[18] E.V. Thuneberg, cond-mat/0005074 (unpublished).

[19] J.M. Karimäki and E.V. Thuneberg, Phys. Rev. B **60**, 15 290 (1999).

[20] In fact, Figs. 2 and 7(b) correspond to $v_n < 0$.

[21] K. Maki and P. Kumar, Phys. Rev. B **17**, 1088 (1978).

[22] E.V. Thuneberg, Physica B **210**, 287 (1995).

[23] Ü. Parts, V.M.H. Ruutu, J.H. Koivuniemi, M. Krusius, E.V. Thuneberg, and G.E. Volovik, Physica B **210**, 311 (1995).